# Validation of computed solids hydrodynamics and pressure oscillations in a bubbling atmospheric fluidized bed

Robert W. Lyczkowski, Isaac K. Gamwo* and Flavio Dobran**
*Argonne National Laboratory, Energy Systems Division, 9700 South Cass Avenue, Argonne, IL 60439 (USA)*

Y. H. Ai, B. T. Chao and M. M. Chen
*University of Illinois at Urbana–Champaign, Department of Mechanical and Industrial Engineering, 1206 West Green Street, Urbana, IL 61801 (USA)*

Dimitri Gidaspow
*Illinois Institute of Technology, Department of Chemical Engineering, Chicago, IL 60616 (USA)*

(Received October 16, 1992; in revised form January 23, 1993)

**Abstract**

The ensemble- and time-averaged solids velocity field and bed dynamics in the form of pressure oscillations taken in the atmospheric 'thin' (3.81 cm×40 cm) bubbling fluidized bed at the University of Illinois at Urbana–Champaign (UIUC) have been analyzed using Argonne National Laboratory's hydrodynamic model FLUFIX implemented on a Cray X-MP/18 supercomputer. The fluidized bed contained a simulated triangular pitch tube array consisting of five, round, 5.08-cm diameter cylinders. The bed material consisted of soda lime glass beads having a narrow size range averaging 460 $\mu$m in diameter. The fluidizing air was introduced at 39 cm $s^{-1}$. Generally correct solids motion is predicted by the FLUFIX computer program. The uncertainties in the UIUC solids motion data varied greatly from location to location; hence, a sensitivity analysis was performed by varying the inlet fluidizing-gas velocity distribution. A convergence study was performed by varying (1) the size of the mesh used to approximate the obstacles and (2) the accuracy of the numerical solution. Essential grid independence is demonstrated for time-averaged axial solids velocities and porosities for the tubes modeled as 2×2 and 4×4 squares and a very tight convergence. Good agreement is obtained for the power spectra of the absolute pressure fluctuations using the fast Fourier transform technique. The computed and experimental major frequencies lie in the relatively narrow range of 2–3 Hz.

## Introduction

Solids motion and the associated bed dynamics involving bubble evolution and pressure fluctuations are the key to understanding the erosion processes in fluidized-bed combustors (FBCs). Fluidized-bed combustors have continued to show promise for burning high sulfur coal, but erosion of in-bed tubes and other components, such as waterwalls, is still hampering the commercialization of the FBC technology. Despite their importance, the exact mechanisms of tube erosion are poorly understood. A major contributing factor to this unsatisfactory state of affairs is the lack of reliable local erosion data as well as the solids impact velocity and impact frequency at the tube surfaces. This problem can, in principle, be resolved as a result of the development of the computer-aided particle-tracking facility (CAPTF) developed at the University of Illinois at Urbana–Champaign by Lin *et al.* [1]. Because erosion is known to be a localized and nonlinear phenomenon, emphasis has been placed on determining the local ensemble- and time-averaged solids velocity and its distribution function on the tube surface. Such information is crucial for the correlation of erosion data.

Argonne National Laboratory (ANL) and the University of Illinois at Urbana–Champaign (UIUC) have collaborated in the Cooperative Research and Development (R&D) Venture, 'Erosion of FBC Heat Transfer Tubes', with the U.S. Department of Energy, Electric Power Research Institute, State of Illinois Center for Research on Sulfur in Coal, Tennessee Valley Authority, ASEA Babcock PFBC, ABB Combustion Engineering Inc., and Foster Wheeler Development Corp. Partici-

*Present address: Carnegie Mellon University, Department of Chemical Engineering, Pittsburgh, PA 15213.
**Present address: New York University, Department of Applied Science, New York, NY 10003.

0032-5910/93/$6.00

pation by the UIUC was made possible by a grant from CRSC. This and other collaborative research by participants in the Cooperative R&D Venture is summarized by Podolski *et al.* [2]. A major objective of the project was to formulate design and operating guidelines to minimize erosion rates in FBCs within their envelope of constraints, e.g. tube bundle geometry, particle diameter and fluidizing velocity.

A key element of this collaborative effort was the development of the hydrodynamic and erosion computer models that were described by Lyczkowki *et al.* [3], Burge [4], and Ding and Lyczkowki [5]. Both two- and three-dimensional time-dependent hydrodynamic computer models are available at ANL. The three-dimensional model, developed by Babcock and Wilcox [4] in close collaboration with ANL, and the three-dimensional kinetic theory model [5] use the same basic solution procedure as the two-dimensional FLUFIX model described by Lyczkowki and Bouillard [6].

UIUC used the CAPTF to obtain the local ensemble- and time-averaged solids velocity data in various fluidized beds containing obstacles. To understand the relationship between the solids motion and the bed dynamics, pressure fluctuations also were measured to deduce the role of bubble dynamics in the erosion process.

Several experimental fluidized beds were designed in accordance with ANL's specifications and approved by the Cooperative R&D Steering Committee. The UIUC fluidized bed used in these analyses contained a simulated triangular-pitch tube array consisting of five, round, 5.08-cm diameter cylinders. This bed is a smaller, thin (3.81 cm), 'two-dimensional' version of the variable thickness erosion experimental bed at Foster Wheeler; that bed consisted of nine tubes in two rows, as discussed by Podolski *et al.* [2]. Whereas Foster Wheeler used 0.15-cm particle diameter molochite in their erosion experiments, the UIUC experiments used glass beads of a narrow size range averaging 460 $\mu$m in particle diameter; in addition to obtaining erosion data, Foster Wheeler also measured absolute and differential pressure fluctuations.

Argonne is using the data obtained from the UIUC fluidized bed experiment described above to perform detailed validation of the FLUFIX computer program. The purpose of this paper is to present the results of the analyses.

## Experimental facilities and procedures

In this section we present a description of the UIUC thin, two-dimensional fluidized-bed experiment and its operating conditions, and also a description of the CAPTF, its operating procedure, and the recently improved calibration setup.

### *Two-dimensional atmospheric fluidized bed and operating conditions*

Figure 1 is an assembly drawing of the two-dimensional atmospheric fluidized bed showing the key dimensions, the inlet of the fluidizing air, and the air plenum. The air distributor is of a box design and packed with 3-mm diameter polyester beads sandwiched between two plexiglass distributor plates, each 3.81 cm × 40 cm and 0.635-cm thick. Both plates are provided with 0.14-cm diameter holes, 0.873-cm center to center spacing, in a staggered arrangement. The top surface of the upper plate is covered with an 80-mesh stainless steel wire gauze, which constitutes the bottom of the bed. The top of the bed was open to the atmosphere.

Figure 2 shows the simulated tube bank and its location in the thin 3.81 cm × 40 cm, two-dimensional, fluidized bed, which consisted of two rows of round cylinders, 5.08 cm in diameter, in a triangular pitch arrangement. The horizontal spacing was 15.2 cm and the vertical spacing was 7.62 cm. The bed material consisted of technical quality soda lime glass beads having a material density of 2 490 kg $m^{-3}$, a size distribution of 425–500 $\mu$m and a mean diameter of 460 $\mu$m. The static bed height was 40.6 cm, and the minimum fluidization velocity, $U_{mf}$, determined from pressure-drop measurements, was 20.4 cm $s^{-1}$. The

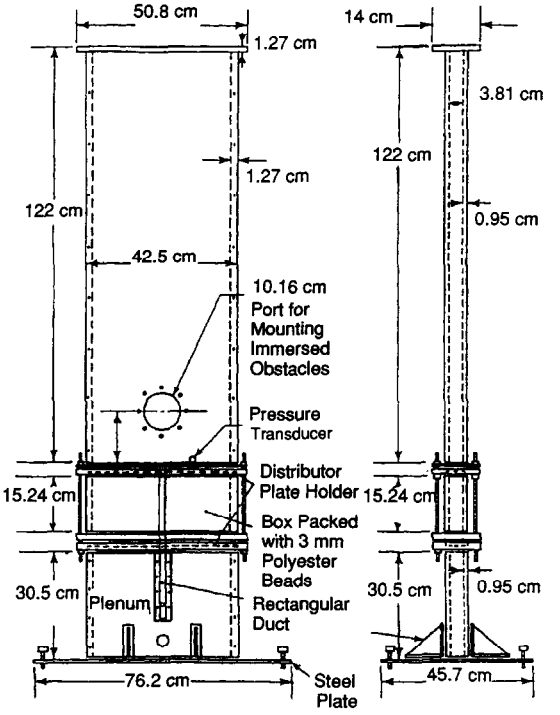


Fig. 1. Assembly drawing of the UIUC two-dimensional atmospheric fluidized bed.

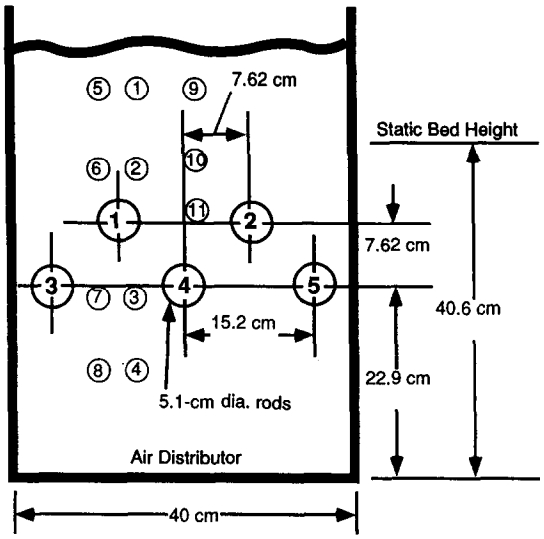


Fig. 2. Schematic diagram of the UIUC two-dimensional fluidized bed showing 5 tubes and 11 pressure measurement locations.

superficial air velocity, $U$, was 39.0 cm $s^{-1}$; thus $U/U_{mf}=1.91$. The five rods are numbered 1 through 5 as shown in Fig. 2. The position of the radioactive tracer was tracked at 5-ms time intervals for a total of 40 h to determine the solids motion. Absolute pressure fluctuations at the 11 locations shown in Fig. 2 were also determined.

The fluidizing air leaving the compressor was dehumidified and filtered to remove oil. Additional filters were installed in the supply line to the two-dimensional bed. The humidity was controlled by diverting a portion of the air flow into a humidifier in which air was forced through a layer of water and then reintroduced into the supply line. The relative humidity, measured by a Vaisala humidity sensor placed in the fluidized bed above the bubbling surface, ranged between 33 and 39%.

*UIUC's computer-aided particle tracking facility (CAPTF)*

The fluidized-bed particle tracking technique is based on continuous tracking of a single radioactive tracer particle that is dynamically identical to the fluidized bed material. As the tracer particle moves with the other particles, its gamma radiation is continuously monitored by 16 strategically arranged scintillation detectors mounted in close proximity to the 40-cm wide surfaces of the bed, 8 at the front and 8 at the rear in a staggered configuration. Using an automatic triangulation scheme described by Lin *et al.* [1], modified to take full advantage of the redundancy provided by the 16 detectors, the instantaneous location of the tracer is determined. The data for the instantaneous locations acquired at 5-ms intervals are time-differenced to yield instantaneous velocities. In earlier experiments [1], the position data were acquired at 30 ms intervals. Mean and fluctuating components of the tracer velocity and the distribution of its occurrence probability are then calculated. A detailed description of the first generation CAPTF was discussed by Lin *et al.* [1].

The radioactive tracer particle was manufactured from a miniature scandium ingot having a specific gravity of 2.89. The scandium particle was coated with a layer of polyurethane of such thickness that the effective density closely matches that of the glass spheres. The diameter of the coated scandium particle was approximately 500 $\mu$m. The coating also prevents the loss of radioactive material in the erosive fluidized-bed environment. Because of the extremely low radiation level of the tracer particle, no special safety precautions were necessary.

As already mentioned, in previous fluidized bed studies, all particle-velocity data were acquired at 30-ms time intervals [1]. A much higher sampling rate was needed for the determination of the velocity distribution functions and the impact frequencies of particles hitting the surfaces of immersed obstacles in the fluidized bed. The impact frequencies are determined by counting the number of times the radioactive tracer particle appears in each of the sampling cells adjacent to the obstacle as it moves toward the surface. The procedure is accurate only if the cell size is sufficiently small. The sampling compartments used in the evaluation of the particle velocities are illustrated in Fig. 3. Included in the figure is the array indexing scheme (I, K). If the particle velocity were as high as the superficial velocity, 39 cm $s^{-1}$, the particle would travel a distance of 1.2 cm; this is larger than the cell size of 4 mm × 10 mm and excessive for the 5.08-cm rods. Hence, all of the position data of the tracer were obtained at 5-ms time intervals, representing a six-fold increase in sampling rate over that used previously.

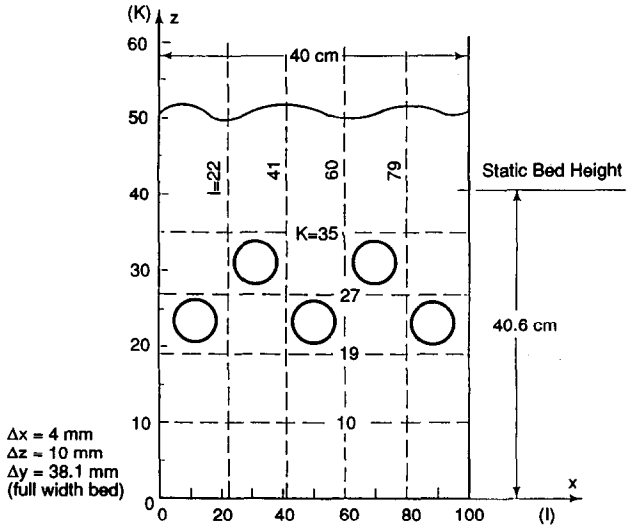


Fig. 3. Sampling compartments for evaluation of solids velocities.

*Improved calibration setup*

The count rate of the gamma rays emitted by the radioactive tracer, and sensed by the NaI crystal of the scintillation counter, depends, for a fixed strength of the radioactivity, on the distance between the tracer and the crystal. The distance versus detector count rate relationship was determined by *in situ* calibration. This procedure consisted of attaching the tracer to the conical tip of a 12.7-mm steel rod held rigidly in a positioning device located above the bubbling surface of the two-dimensional bed. The calibration rod was thus a simple cantilever. However, when the length of the cantilever was too long, its tip oscillated under the action of the fluctuating pressure and solids motion in the fluidized bed, thus contributing error to the calibration data. This shortcoming was, to a great extent, remedied by providing additional support. The rod has, in essence, been converted from a cantilever to a simple beam with two clamped supports and an overhang. As a result, the rigidity of the rod was greatly increased, and a 2- to 3-fold reduction in the scatter of the calibration data was noticed.

## Experimental results

Experimental results were obtained for (1) the ensemble- and time-averaged solids velocity field, (2) directional distribution functions of particles hitting selected surfaces of several rods, (3) velocity distribution functions of particles hitting these surfaces in a number of selected directions, and (4) spectral analysis of the absolute pressure fluctuations. Because the emphasis in this paper is the analysis of items (1) and (4), only these results will be presented. The motivation and utility of the rest of the data comprising items (2) and (3) as they relate to erosion mechanisms will now be briefly explained.

*Ensemble- and time averaged solids velocity field*

The ensemble- and the time-averaged solids velocity data components were received by ANL from UIUC and plotted using a modification of the post-processing graphics computer program used for FLUFIX hydrodynamic calculations. The solids velocity vector plots are shown in Fig. 4. The data are plotted using two different velocity scales, 5 and 10 cm $s^{-1}$, as indicated by the small arrows near the upper right of each plot. Plotting of the solids velocity vectors was suppressed above a bed height of 52 cm ($K=52$) because the number of occurrences dropped below 100, causing erroneous results. It was not possible to plot every one of the velocity magnitudes because of the large number of compartments (100 in the $x$ direction and 60 in the $z$ direction totaling 6 000 compartments) used in the

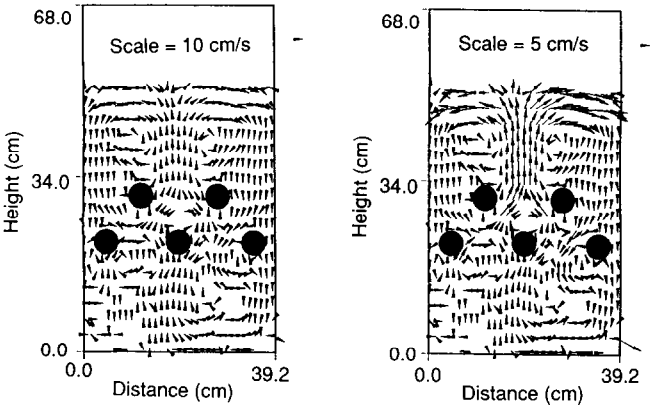


Fig. 4. Experimental ensemble- and time-averaged solids velocity vector plots.

data reduction as shown in Fig. 3. Every third velocity vector was plotted in the $x$ direction and every second velocity vector was plotted in the $z$ direction in Fig. 4. The complete set of data for the compartments consisting of the two velocity components and the associated number occurrences is available [7].

The general solids motion follows a 'gulf-stream' pattern, with solids rising upward in the middle of the bed and falling downward near the side walls [8]. Complicated patterns exist in the vicinity of the simulated tube array with a more or less clockwise circulation around tube 2 and counterclockwise around tube 1. Overall, the velocity vector field is close to being symmetric except in regions of very low velocity near the distributor. The circulation pattern below the simulated tube bank is roughly a countercurrent vortex motion. It is clear from examination of the two plots in Fig. 4 that the maximum solids velocity is about 10 cm $s^{-1}$ near the middle of the bed above tube 4 and in the vicinity of the expanded bed height.

If it is assumed that the solids bulk density is directly related to the occurrence number of the tracer, then it is possible to examine the self-consistency of the measured data by calculating the *net* mass flow through four imaginary horizontal surfaces extending over the entire cross section of the bed and four imaginary vertical surfaces of sufficient height. Ideally, the net mass flux should be zero because of the circulatory motion of the solids, none of which leave the fluidized bed. The results of this calculation showed that the deviation from the ideal condition amounted to a few percent [7].

*Confidence level of averaged data*

In the particle-tracking technique, it is assumed that the measured Lagrangian (following the particles) velocities of the tracer in any given sampling compartment are random variables. The ensemble-average can be taken to be the time-average of the solids' Eulerian

(fixed in space) velocities in that compartment if the sample size is infinitely large. The velocities of the tracer determined for each of its repeated occurrences in a given compartment can be assumed to be mutually independent as the relaxation time for momentum transfer is very much smaller than the time elapsed between the tracer's exit and its reentry into the compartment. If the entire data set is subdivided into a finite number of subsets, then the mean and the variance of the entirety of the data are the same as the mean and variance of the subsets provided, again, that the size of the sampled data is infinitely large. When the sample size is not infinitely large, the ratio of the standard deviation to the mean of the mean values of the subsets provides a measure of the confidence level of the ensemble-averaged velocities. The number of occurrences of the tracer in a sampling compartment per unit time are also random variables and may be treated in a similar manner.

The foregoing method of analysis has been applied to the data collected for the number of occurrences and for the velocity of the tracer in six sampling compartments of two categories. Category A consists of three compartments having high occurrence numbers, and Category B consists of three compartments having low occurrence numbers. We shall soon demonstrate that the confidence level of the averaged velocity data drops sharply when the occurrence number is low. This, of course, is expected, but quantitative data have not been previously reported. Referring to Fig. 3, the compartments in Category A are [$I=45$, $K=40$], for which the tracer's velocity has a dominant vertical component; [$I=45$, $K=30$], for which the vertical and horizontal components of the tracer's velocity are nearly equal; and [$I=28$, $K=48$], for which the tracer's velocity has a dominant horizontal component. The results are summarized in Table 1(a). In the table, the subsets referred to in the preceding paragraph are designated by j (1 to 8), and each contains data collected during five hours of experimental run. Other quantities in the table are defined as follows: $L_j$ = number of tracer's occurrences per hour, $V_{xj}$ and $V_{zj}$ = $x$ and $z$ components of the tracer's velocity, $|V|$ = speed of the tracer, and $\theta$ = direction of the velocity vector as measured in the counterclockwise direction from the positive direction of the $x$ axis. In assessing the variability of the averaged velocity data, we evaluate the mean and the standard deviation of the particles' speed $|V|$ and the direction of the velocity vector $\theta$ instead of the two velocity components. The numerical value of $\theta$ depends on the reference direction from which $\theta$ is measured, and the selection of the reference direction is arbitrary. Hence, only the standard deviation, $\sigma_\theta$, is tabulated instead of the ratio $\sigma_\theta/\bar{\theta}$. The confidence level of the averaged velocity data is high when both $\sigma_{|V|}/|\bar{V}|$ and $\sigma_\theta$ are small. Although the velocity data for the three locations are judged to be acceptable, it is not known why the data for location [$I=45$, $K=40$] are inferior to those for [$I=45$, $K=30$] and [$I=28$, K=48].

We now turn to Category B and examine the variability in the averaged data when the occurrence is low. The three compartments selected for this purpose are: [$I=47$, $K=53$], [$I=95$, $K=5$], and [$I=89$, $K=52$]. The results are summarized in Table 1(b). For all three compartments, both the ratio $\sigma_{|V|}/|\bar{V}|$ and $\sigma_\theta$ are unacceptably large. Although it is debatable if the averaged data based on the entire 40-h run may still be used for our present purpose, it is unlikely that any data based on the 5-h run could be useful.

*Directional and speed distribution functions of particles hitting simulated tube bank*

Lyczkowski *et al.* [3] compared erosion models for a few-tube approximation of the Coal Research Establishment's cold atmospheric model of the IEA Grimethorpe tube bank 'C1' and found that the rate of tube erosion increases with increasing gas fluidizing velocity. Of interest is the indication that erosion ceases at $U/U_{mf}$ values of approximately 0.8. They also studied the influence of solids impingement angle on the erosion rates of aluminum tubes impacted by aluminum oxide particles using the Nielson and Gilchrist [9] model. It was found that, for a fixed speed, maximum erosion rates occurred at an impingement angle of about 20° (or 70° from the normal). Hence, the directional distribution functions of particles hitting the various surfaces of immersed rods of the simulated tube bank were determined. The directional distribution function describes how the particles hitting the surface distribute among themselves in the two-dimensional half-space external to the surface. The data were analyzed in two ways: first, particles of all speeds were counted and, second, only particles with speeds greater than $0.8U_{mf}$ ($\sim 16$ cm s$^{-1}$) were counted. Differences were noted for the two cases, indicating that there is a significant redistribution when the existence of a threshold velocity is recognized.

The information contained in the directional distribution functions is obviously important with respect to understanding erosion mechanisms, but it is incomplete. As has been pointed out by Lyczkowski *et al.* [3], erosion by a stream of particles depends not only on the direction of impingement, but also on the impaction speed. Such information is embodied in the speed distribution function. It describes how the speed of particles hitting a surface in a given direction is distributed. This information, together with the directional distribution function, is potentially useful in understanding erosion mechanisms. Samples of directional and speed distribution functions of a 500-$\mu$m tracer hitting rod 1 of

TABLE 1(a). Uncertainties in ensemble-averaged particle velocities for compartments having high occurrence numbers

| Location [$I=45$, $K=40$] Set j | 1 | 2 | 3 | 4 | 5 | 6 | 7 | 8 |
|---|---|---|---|---|---|---|---|---|
| $L_j$, #/h$^{-1}$ | 128 | 131 | 121 | 131 | 124 | 164 | 127 | 163 |
| $V_{xj}$, cm s$^{-1}$ | −0.25 | 0.21 | 0.17 | −1.04 | −0.94 | −0.75 | −1.51 | 1.15 |
| $V_{zj}$, cm s$^{-1}$ | 17.66 | 10.58 | 16.34 | 11.38 | 8.25 | 9.61 | 5.31 | 9.63 |
| $\|V\|$, cm s$^{-1}$ | 17.66 | 10.58 | 16.34 | 11.43 | 8.30 | 9.64 | 5.52 | 9.70 |
| $\Theta$, deg | 90.81 | 88.86 | 89.40 | 95.22 | 96.50 | 94.46 | 105.87 | 83.19 |

| $\bar{L}$ | $\sigma_L$ | $\sigma_L/\bar{L}$ | $\|\bar{V}\|$ | $\sigma_{\|V\|}$ | $\sigma_{\|V\|}/\|\bar{V}\|$ | $\bar{\Theta}$ | $\sigma_\Theta$ |
|---|---|---|---|---|---|---|---|
| 136 h$^{-1}$ | 17 h$^{-1}$ | 13% | 11.15 cm s$^{-1}$ | 3.95 cm s$^{-1}$ | 35% | 93.0 deg | 6.7 deg |

| Location [$I=45$, $K=30$] Set j | 1 | 2 | 3 | 4 | 5 | 6 | 7 | 8 |
|---|---|---|---|---|---|---|---|---|
| $L_j$, #/h$^{-1}$ | 110 | 114 | 143 | 108 | 179 | 127 | 125 | 146 |
| $V_{xj}$, cm s$^{-1}$ | 5.19 | 4.40 | 4.09 | 5.24 | 5.00 | 5.07 | 4.84 | 4.06 |
| $V_{zj}$, cm s$^{-1}$ | 4.11 | 4.57 | 3.72 | 3.86 | 4.17 | 3.77 | 4.37 | 3.98 |
| $\|V\|$, cm s$^{-1}$ | 6.62 | 6.34 | 5.53 | 6.51 | 6.51 | 6.32 | 6.52 | 5.69 |
| $\Theta$, deg | 38.38 | 46.09 | 42.29 | 36.38 | 39.83 | 36.63 | 42.08 | 44.43 |

| $\bar{L}$ | $\sigma_L$ | $\sigma_L/\bar{L}$ | $\|\bar{V}\|$ | $\sigma_{\|V\|}$ | $\sigma_{\|V\|}/\|\bar{V}\|$ | $\bar{\Theta}$ | $\sigma_\Theta$ |
|---|---|---|---|---|---|---|---|
| 132 h$^{-1}$ | 24 h$^{-1}$ | 18% | 6.26 cm s$^{-1}$ | 0.41 cm s$^{-1}$ | 7% | 40.8 deg | 3.6 deg |

| Location [$I=28$, $K=48$] Set j | 1 | 2 | 3 | 4 | 5 | 6 | 7 | 8 |
|---|---|---|---|---|---|---|---|---|
| $L_j$, #/h$^{-1}$ | 96 | 122 | 110 | 105 | 93 | 117 | 90 | 120 |
| $V_{xj}$, cm s$^{-1}$ | −11.69 | −10.47 | −8.92 | −12.15 | −9.43 | −11.60 | −12.90 | −9.16 |
| $V_{zj}$, cm s$^{-1}$ | −0.23 | 0.68 | −0.15 | 0.52 | 0.81 | −0.10 | 0.58 | 0.27 |
| $\|V\|$, cm s$^{-1}$ | 11.69 | 10.49 | 8.92 | 12.16 | 9.46 | 11.60 | 12.91 | 9.16 |
| $\Theta$, deg | 181.13 | 176.30 | 180.96 | 177.55 | 175.09 | 180.49 | 177.43 | 181.69 |

| $\bar{L}$ | $\sigma_L$ | $\sigma_L/\bar{L}$ | $\|\bar{V}\|$ | $\sigma_{\|V\|}$ | $\sigma_{\|V\|}/\|\bar{V}\|$ | $\bar{\Theta}$ | $\sigma_\Theta$ |
|---|---|---|---|---|---|---|---|
| 107 h$^{-1}$ | 13 h$^{-1}$ | 12% | 10.80 cm s$^{-1}$ | 1.50 cm s$^{-1}$ | 14% | 178.8 deg | 2.5 deg |

the simulated tube bank shown in Fig. 2 are given in Podolski *et al.* [2]. More complete and comprehensive data can be found in the thesis by Ai [7].

*Power spectral analysis of static pressure fluctuations*

After the 40-h test run was completed, static pressure fluctuations were obtained using a PCB Piezotronics acceleration-compensated, miniature, quartz transducer. It has overall dimensions of approximately 6.4-mm diameter and 35-mm length. The probe, as delivered, has a resolution of 27.6 Pa and a rise time of 2 $\mu$s. An extended metal cap in the form of a cylindrical cavity was mounted at the probe end. Three 1-mm diameter holes, 120° apart, were drilled through the cylindrical wall of the cap and covered with 80-mesh gauze. The sampling frequency was 30 Hz. For each measurement location, the autocorrelation was first evaluated from the fluctuating pressure using the fast Fourier transform (FFT) technique to obtain the power spectra. Results were obtained at the 11 locations shown in Fig. 2. Power spectra for locations 6 and 7 are shown in Fig. 5 with ordinates plotted in relative scale only. From these two figures, as well as the other nine, it was quite clear that the dominant frequencies for all locations fell within the narrow range of 2–3-Hz. However, the amplitudes varied greatly indicating a wide range of energies; the higher the amplitude, the greater the energy. These findings extend prior information concerning pressure fluctuations in bubbling fluidized bed, see for example Sitnai and Whitehead [10].

## Hydrodynamic model

Hydrodynamic models of fluidization use the principles of conservation of mass, momentum, and energy. The general mass conservation equations and the separate phase momentum equations for transient and isothermal fluid-solids, nonreactive, multiphase flow (in vector notation) are written as follows in conservation

TABLE 1(b). Uncertainties in ensemble-averaged particle velocities for compartments having low occurrence numbers

| Location [$I=47$, $K=53$] Set j | 1 | 2 | 3 | 4 | 5 | 6 | 7 | 8 |
|---|---|---|---|---|---|---|---|---|
| $L_j$, #/h$^{-1}$ | 18 | 20 | 34 | 32 | 16 | 16 | 18 | 26 |
| $V_{xj}$, cm s$^{-1}$ | 8.22 | 21.37 | 8.45 | −13.33 | −2.56 | −10.51 | −4.89 | −0.30 |
| $V_{zj}$, cm s$^{-1}$ | 7.56 | −8.53 | 13.93 | −3.70 | 11.54 | 17.69 | 12.00 | 11.52 |
| $\|V\|$, cm s$^{-1}$ | 11.17 | 23.01 | 16.29 | 13.83 | 11.82 | 20.58 | 12.96 | 11.52 |
| $\Theta$, deg | 42.60 | 338.24 | 58.76 | 195.51 | 102.51 | 120.72 | 112.17 | 91.49 |

| $\bar{L}$ | $\sigma_L$ | $\sigma_L/\bar{L}$ | $\|\bar{V}\|$ | $\sigma_{\|V\|}$ | $\sigma_{\|V\|}/\|\bar{V}\|$ | $\bar{\Theta}$ | $\sigma_\Theta$ |
|---|---|---|---|---|---|---|---|
| 23 h$^{-1}$ | 7 h$^{-1}$ | 30% | 15.15 cm s$^{-1}$ | 4.48 cm s$^{-1}$ | 30% | 87.8 deg | 63.7 deg |

| Location [$I=95$, $K=5$] Set j | 1 | 2 | 3 | 4 | 5 | 6 | 7 | 8 |
|---|---|---|---|---|---|---|---|---|
| $L_j$, #/h$^{-1}$ | 35 | 31 | 17 | 10 | 8 | 35 | 25 | 32 |
| $V_{xj}$, cm s$^{-1}$ | −1.15 | −1.41 | −5.24 | −0.83 | −3.81 | −5.06 | −1.11 | −3.95 |
| $V_{zj}$, cm s$^{-1}$ | −4.14 | −2.44 | −10.95 | 4.58 | −13.81 | 0.11 | 0.00 | −2.96 |
| $\|V\|$, cm s$^{-1}$ | 4.29 | 2.82 | 12.14 | 4.65 | 14.33 | 5.06 | 1.11 | 4.94 |
| $\Theta$, deg | 254.48 | 239.98 | 244.43 | 100.27 | 254.58 | 178.75 | 180 | 216.85 |

| $\bar{L}$ | $\sigma_L$ | $\sigma_L/\bar{L}$ | $\|\bar{V}\|$ | $\sigma_{\|V\|}$ | $\sigma_{\|V\|}/\|\bar{V}\|$ | $\bar{\Theta}$ | $\sigma_\Theta$ |
|---|---|---|---|---|---|---|---|
| 24 h$^{-1}$ | 11 h$^{-1}$ | 46% | 6.17 cm s$^{-1}$ | 4.59 cm s$^{-1}$ | 74% | 208.7 deg | 53.5 deg |

| Location [$I=89$, $K=52$] Set j | 1 | 2 | 3 | 4 | 5 | 6 | 7 | 8 |
|---|---|---|---|---|---|---|---|---|
| $L_j$, #/h$^{-1}$ | 16 | 25 | 26 | 11 | 16 | 7 | 13 | 26 |
| $V_{xj}$, cm s$^{-1}$ | 16.41 | 8.73 | 6.36 | 11.85 | 6.67 | 6.11 | 25.15 | 17.88 |
| $V_{zj}$, cm s$^{-1}$ | 15.64 | 0.48 | −2.88 | −6.30 | 6.41 | 5.56 | −1.21 | −3.64 |
| $\|V\|$, cm s$^{-1}$ | 22.67 | 8.74 | 6.98 | 13.42 | 9.25 | 8.26 | 25.18 | 18.25 |
| $\Theta$, deg | 43.62 | 3.15 | 335.64 | 332.00 | 43.86 | 42.30 | 357.25 | 348.49 |

| $\bar{L}$ | $\sigma_L$ | $\sigma_L/\bar{L}$ | $\|\bar{V}\|$ | $\sigma_{\|V\|}$ | $\sigma_{\|V\|}/\|\bar{V}\|$ | $\bar{\Theta}$ | $\sigma_\Theta$ |
|---|---|---|---|---|---|---|---|
| 18 h$^{-1}$ | 8 h$^{-1}$ | 44% | 14.09 cm s$^{-1}$ | 7.08 cm s$^{-1}$ | 50% | 8.7 deg | 30.2 deg |

law form for two hydrodynamic models (refer to the List of Symbols section for definition of terms):

Continuity

$$\frac{\partial}{\partial t}(\epsilon_k\rho_k)+\nabla\cdot(\epsilon_k\rho_k\vec{v}_k)=0 \text{ and} \tag{1}$$

Momentum

$$\frac{\partial}{\partial t}(\epsilon_k\rho_k\vec{v}_k)+\nabla\cdot(\epsilon_k\rho_k\vec{v}_k\vec{v}_k)$$

Acceleration

$$=\nabla\cdot\bar{\bar{\sigma}}_{ke}+\epsilon_k\rho_k\vec{g}+\sum_{i=1}^{n}\bar{\bar{\beta}}_{ik}\cdot(\vec{v}_i-\vec{v}_k) \tag{2}$$

Stress Gravity Interphrase Drag

Each phase is denoted by the subscript k and the total number of phases is $n$.

The effective stress tensor, $\bar{\bar{\sigma}}_{ke}$, contains pressure, viscous, and coulombic components, according to the convention [11],

$$\nabla\cdot\bar{\bar{\sigma}}_{ke}=\begin{cases}-\epsilon_k\nabla\cdot(P\bar{\bar{I}})+\nabla\cdot(\epsilon_k\bar{\bar{\tau}}_{kv})-\delta_{ksi}\nabla\cdot\bar{\bar{\tau}}_{kc} & \text{(3a)}\\ \quad\text{(Hydrodynamic Model A)}\\ -(1-\delta_{ksi})\nabla\cdot(P\bar{\bar{I}})+\nabla\cdot(\epsilon_k\bar{\bar{\tau}}_{kv})-\delta_{ksi}\nabla\cdot\bar{\bar{\tau}}_{kc} & \text{(3b)}\\ \quad\text{(Hydrodynamic Model B)}\end{cases}$$

The Kronecker delta function, $\delta_{ksi}$, is given by

$$\delta_{ksi}=\begin{cases}1 \text{ if } k=s_i, \text{ or}\\ 0 \text{ if } k\neq s_i\end{cases} \tag{4}$$

where $k=s_i$ is a solids phase.

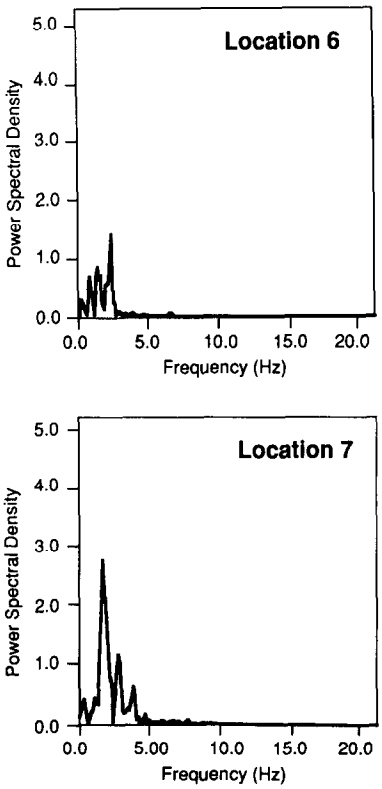


Fig. 5. Experimental static pressure fluctuation power spectra for locations 6 and 7.

The solids elastic modulus, $G(\epsilon_k)$, is defined as the normal component of the solids coulombic stress through the following relationship [11, 12]:

$$\nabla \cdot \bar{\bar{\tau}}_{kc} = G(\epsilon_k)\bar{\bar{I}} \cdot \nabla \epsilon_k \tag{5}$$

where $\bar{\bar{I}}$ is the unit tensor. $G(\epsilon_k)$ is the only component of the solids coulombic stress used at present. For a two-phase fluid/solids mixture, eqn. (5) becomes

$$\nabla \cdot \bar{\bar{\tau}}_{sc} = G(\epsilon_s)\bar{\bar{I}} \cdot \nabla \epsilon_s = -G(\epsilon_s)\bar{\bar{I}} \cdot \nabla \epsilon \tag{6}$$

Simple semi-empirical theory was used to develop a generic form of the solids elastic modulus [6] that may be written as

$$G(\epsilon_s)/G_0 = \exp[c(\epsilon_s - \epsilon_s^*)] = \exp[-c(\epsilon - \epsilon^*)] \tag{7}$$

In this study, we use $c = 600$ and $G_0 = 1.0$ Pa. The gas density is evaluated using the ideal gas law [6].

The viscous stress terms are given by

$$\bar{\bar{\tau}}_{kv} = 2\mu_k \bar{\bar{D}}_k - \frac{2}{3}\mu_k \nabla \cdot \vec{v}_k \bar{\bar{I}} \tag{8}$$

where the deformation tensor $\bar{\bar{D}}_k$ is given by

$$\bar{\bar{D}}_k = \frac{1}{2}[\nabla \vec{v}_k + (\nabla \vec{v}_k)^T]. \tag{9}$$

Both hydrodynamic models A and B given by eqns. (2), (3a), and (3b), together with accepted expressions for the interphase drag, have been evaluated by comparison with experimental data taken in a very similar thin two-dimensional fluidized bed containing a rectangular obstacle [3, 11, 13].

Gidaspow's [12] review of the historical background of hydrodynamic models of fluidization contains an extensive bibliography which complements Jackson's review [14]. The value of the computer model lies in its demonstrated ability to successfully predict bubble sizes and time-averaged porosity distributions [12, 13]. The value of the computer model would be enhanced if it could be further validated using the ensemble- and time-averaged solids velocity and static pressure fluctuation data described in the experimental results section.

## Numerical convergence and accuracy study

Before analyzing the ensemble- and time-averaged solids velocity data and power spectra of the static pressure fluctuations, a careful study was performed to assess the numerical convergence and accuracy of the computations. This is a necessary step in any computer modeling exercise. It also served to shed light on the potential experimental uncertainties in the fluidizing air boundary condition.

The FLUFIX models shown in Fig. 6 model the round tubes as squares, with $18 \times 42 = 756$ total cells in one model and $34 \times 82 = 2\,788$ total cells in the other. These totals include the 'dummy' cells around the periphery of the physical boundary. The number of computational cells is therefore $16 \times 40 = 640$ and $32 \times 80 = 2\,560$. We will refer to these two meshes as the 'coarse' and 'fine'. The square obstacles are 5.08 cm $\times$ 5.08 cm on a side, with equal size meshes in each direction – $2 \times 2$ for the coarse and $4 \times 4$ for the fine. No assumption of symmetry was made.

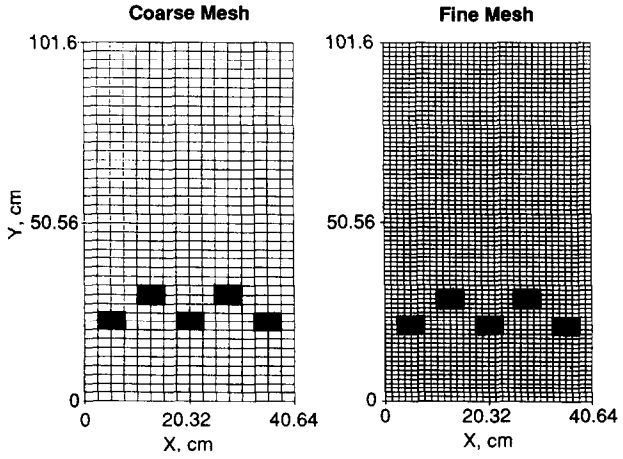


Fig. 6. Computational meshes used in the convergence study.

The conditions of the experimental simulation are given in Table 2. The inlet superficial gas velocity was first maintained at $0.9U_{mf}$ for 1.0 s, where $U_{mf}$ was taken to be 19.5 cm $s^{-1}$ as determined from the Ergun equation programmed in the FLUFIX [6] computer program. This was done to obtain a reasonable initial condition for the subsequent run at $U/U_{mf}=2.0$. The compaction gas volume fraction in eqn. (7) was set equal to 0.39 to accomplish this. The timestep used in all the runs was $5\times10^{-5}$ s. Hydrodynamic Model B was used with a solids viscosity of 0.1 Pa s (1.0 poise) and a gas viscosity of $1.82\times10^{-5}$ Pa s ($1.82\times10^{-4}$ poise).

First, the time required for time-averaging the transient calculations was determined. Very little difference in results could be seen using time-averaging periods of 1–4 s. Therefore, all subsequent results presented herein are averaged over 1 s.

Figures 7 and 8 show qualitative comparisons of loose and tight convergence for the coarse (2×2) and fine

TABLE 2. CAPTF five tube fluidized-bed experiment simulation operating conditions

| | |
|---|---|
| bed material | glass beads |
| particle mean diameter, cm | 0.046 |
| particle density, kg $m^{-3}$ | $2.49\times10^3$ |
| particle sphericity | 1.0 |
| minimum fluidization porosity | 0.41 |
| fluid carrier | Air |
| temperature, K | 300 |
| pressure at top of bed, kPa | 101.3 |
| minimum fluidization velocity, $U_{mf}$, cm $s^{-1}$ | 19.5 |
| fluidizing velocity, $U$, cm $s^{-1}$ | 39.0 |
| $U/U_{mf}$ | 2.0 |

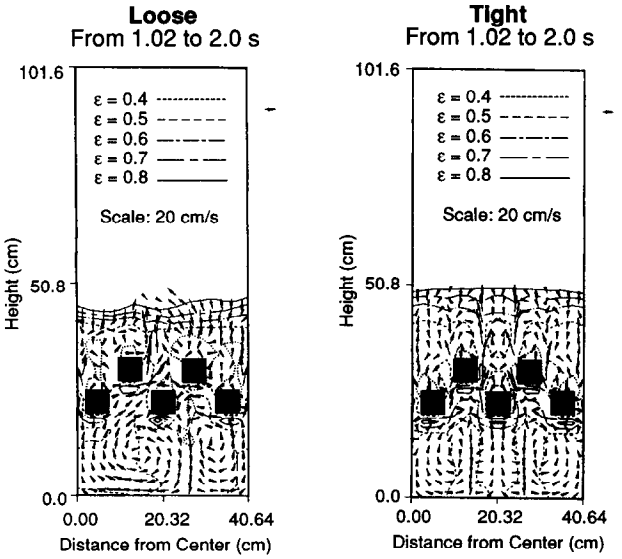


Fig. 7. Computed time-averaged porosity contour and solids velocity vector plots for coarse (2×2) mesh — effect of convergence criteria.

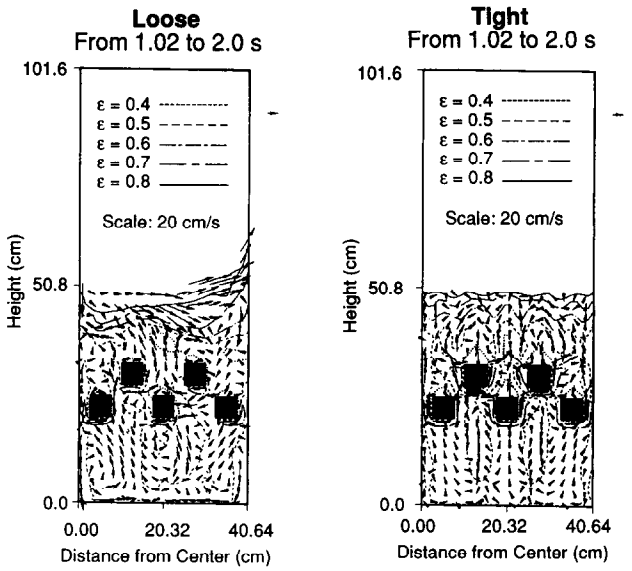


Fig. 8. Computed time-averaged porosity contour and solids velocity vector plots for fine (4×4) mesh — effect of convergence criteria.

(4×4) mesh computer models, respectively. There are clearly differences between the results, with the tight convergence results agreeing more closely with each other. The definition of loose convergence is the FLUFIX code [6] default value, $5\times10^{-4}$, and tight convergence is a value of $10^{-7}$, 3.5 orders of magnitude more accurate. The convergence parameter controls the pressure-adjustment iteration and depends on how well the gas-phase continuity equation is satisfied [6]. With a tight convergence, much more accurate local mass balances are achieved. It is recommended that tight convergence be used in all future simulations. The tight convergence results are decidedly more symmetric than the loose convergence results. However, they differ from the data shown in Fig. 4. The tight-convergence fine-mesh results in Fig. 8 display a counter clockwise circulation pattern around tube 2, whereas the data indicate a clockwise pattern. (The remedy for such data differences will be explained in the next section.)

A quantitative comparison of the loose- and tight-convergence time-averaged porosities and axial solids velocities in Figs. 9 and 10 for the plane passing through tubes 2 and 5 ($x=31.75$ cm) for the coarse and fine meshes. Figure 9 shows that larger bubbles are formed in the vicinity of both of these tubes (height = 20 and 30 cm) for the tight-convergence case. There are fewer differences between the fine- and coarse-mesh results for tight convergence than for loose convergence. On the whole, the porosity profiles are quite similar.

A much more sensitive test of convergence and accuracy is comparing the solids velocities. This is done in Fig. 10 at the same location. As can be seen, there

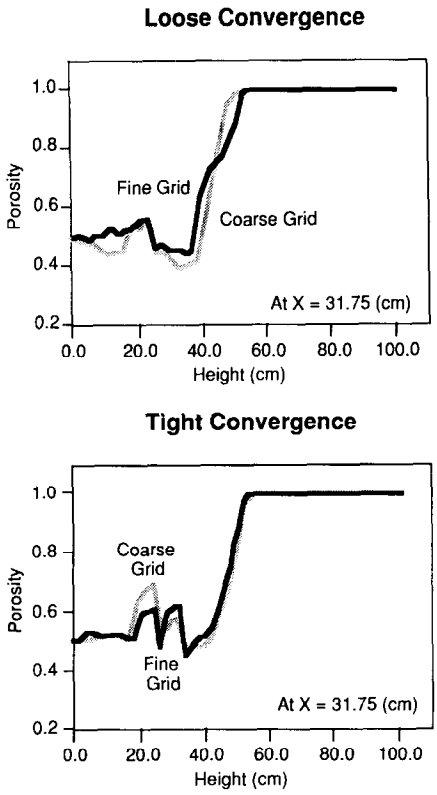


Fig. 9. Computed time-averaged vertical porosity profiles — effect of grid size.

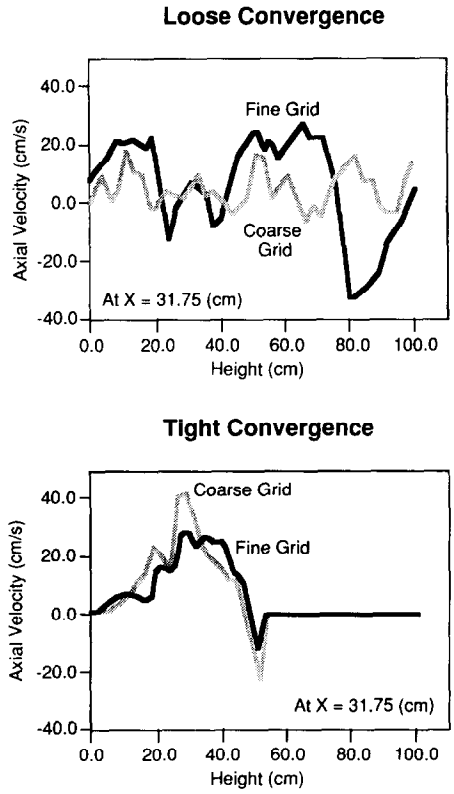


Fig. 10. Computed time-averaged vertical solids axial velocity profiles — effect of grid size.

is a great deal of difference between the coarse- and fine-mesh results. However, the tight-convergence results are basically identical. The axial solids velocities between the tubes are larger than the data. (This discrepancy will also be discussed in the next section.)

Thus, we have proven that essentially converged results can be obtained with a coarse mesh and tight convergence.

## Comparison with experimental data

In order to evaluate the validity of the above model, both the predicted solids flow patterns and axial solids velocity were compared with the experimental data. As discussed in the section entitled 'Numerical convergence and accuracy study', although an essentially grid-independent solution was achieved, the solids velocity patterns predicted differed from the experimental data. Because the standard deviation of the solids velocity data differed significantly from position to position in the bed, it was suspected that there were nonuniformities in the inlet-gas distribution. On the basis of physical arguments, it was decided to increase the inlet-gas flow in the central portion of the bed. This is reasonable because solids tend to come down the sidewalls, obstructing the gas flow there. The gas flow in the central half was increased 30% from the average, and the gas flow near the sidewalls was decreased 30%, so that the total gas flow was the same as in the experiment. Most of the solids flow patterns now agreed qualitatively with the CAPTF data, but they did not agree quantitatively. Although the possibility for inlet-gas flow nonuniformities may exist, it was therefore ruled out as the major reason for the disagreement with the data.

Rietema [15] conducted an exhaustive literature survey for the effective solids viscosity. In our model, this corresponds to $\epsilon_s \mu_s$. He concluded that the value is on the order of 0.01 to 1.0 Pa s (0.1 to 10 poise), and that it decreases with increasing gas fluidizing velocity (increasing porosity) and decreases with decreasing mean particle diameter. For the conditions closest to those in the present experiment, a value of 5.9 Pa s (59 poise) is reported by Singh *et al.* [16]. A value for microscopic solids viscosity of 5 Pa s (50 poise) was chosen. The maximum effective solids viscosity is therefore $0.59 \times 5.0$ Pa s $= 2.95$ Pa s (29.5 poise).

Figure 11 shows good qualitative agreement between the computed time-averaged solids flow pattern and the measured data for uniform inlet air superficial velocity. Both the experiment and the prediction show solids generally ascending near the bed center and descending near the side walls. The weak vortex pattern observed in the experiment in the lower right part of the bed is predicted. Thus, there exist two sets of gulf

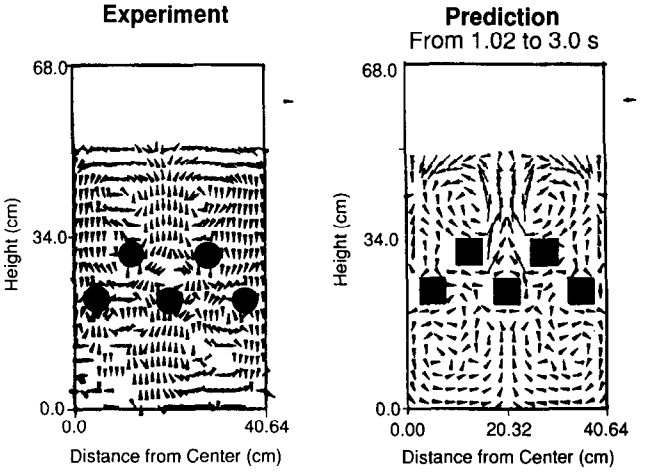


Fig. 11. Comparison of experimental and computed solids flow patterns.

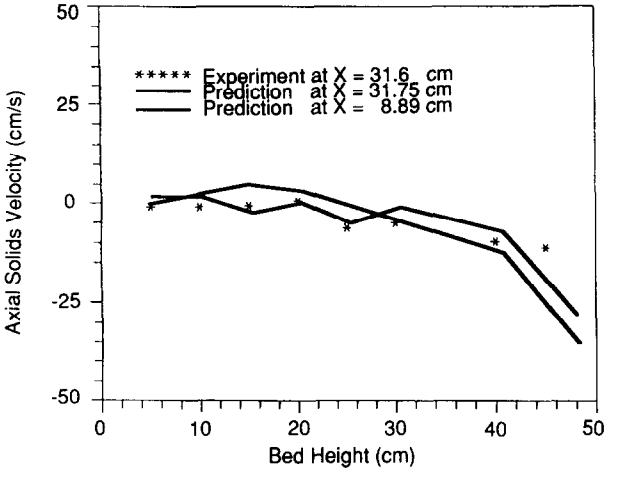


Fig. 12. Comparison of computed and experimental vertical solids axial velocity profiles at $X=31.6$ cm.

streams: one below the tubes and one above the tubes. The experimental and predicted bed expansions are in excellent agreement.

Figure 12 is a comparison of the axial solids velocity profiles computed at $x=8.89$ cm and $x=31.75$ cm with the experimental values. Excellent agreement exists between the data and the computations. However, as can be seen in Fig. 13, in the vicinity of the tubes, at bed height from approximately 20 to 40 cm, the axial solids velocity profiles are higher than the data.

The power spectra of the computed pressure fluctuations are shown in Fig. 14 for the coarse mesh and tight convergence. As can be seen by comparison with Fig. 5, the agreement is quite close. The major frequencies predicted by the simulation are in the range of 2–3 Hz, in agreement with the data. Also predicted is a secondary lower frequency of about 1 Hz. For location 7, a major frequency of 2 Hz is predicted while the data indicated 1.6 Hz. The bandwidth is somewhat

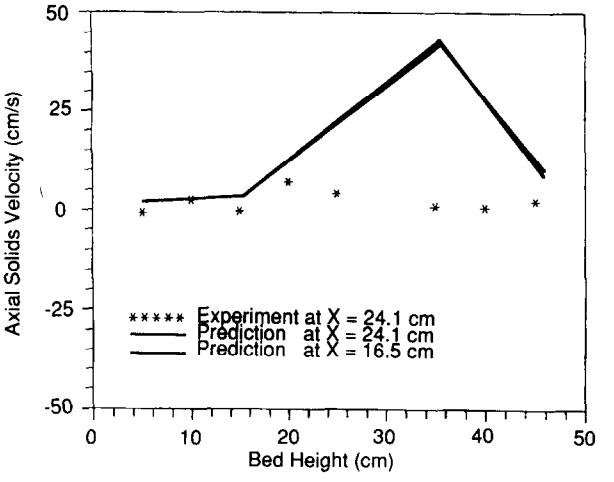


Fig. 13. Comparison of computed and experimental vertical solids axial velocity profiles at $X=24.1$ cm.

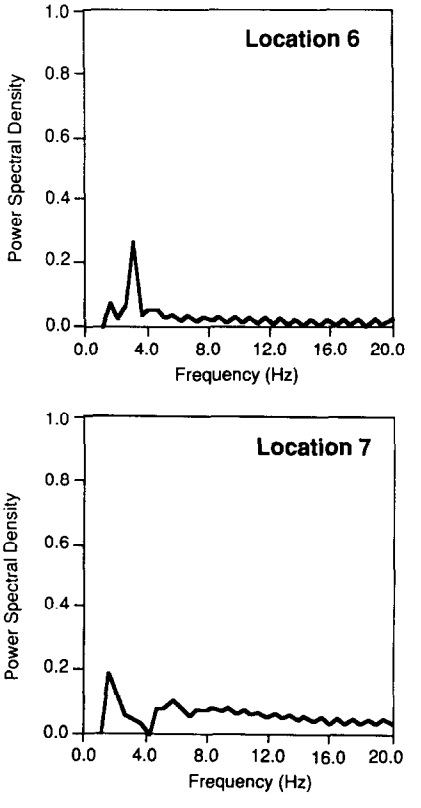


Fig. 14. Computed static pressure fluctuation power spectra for locations 6 and 7.

higher for location 7 than for location 6 for both the experimental data and the model predictions. As it was for the data, the major frequencies predicted for the model for the 11 locations varied in a narrow range of from 2 to 3 Hz.

Figure 15 shows the porosity distributions, represented by dot plots, at three progressive times. At 0.905 s, the bubbles have already formed. These bubbles move upward as time progresses ($t=0.965$ s) and burst at

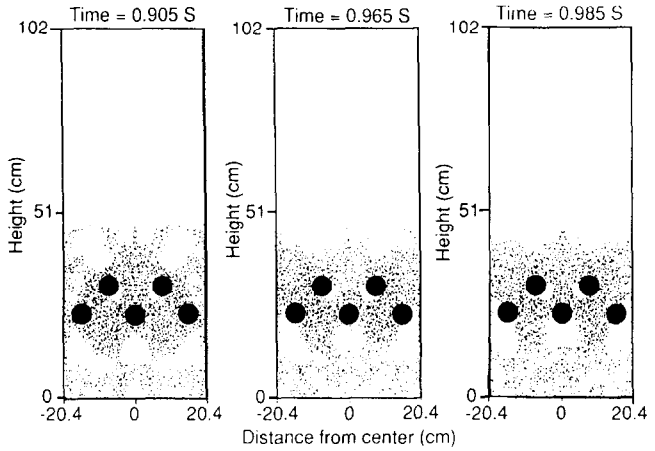


Fig. 15. Computer-generated porosity distributions at three progressive times.

the bed surface ($t=0.985$ s). Then the bed collapses to its initial height and expands again as the cycle appears to repeat itself.

Because the major frequency is 2–3 Hz, and the spacing between the tubes is about 10 cm, one would expect a bubble rise velocity in the vicinity of the tubes of about 20–30 cm $s^{-1}$. One would also expect a solids velocity comparable to this bubble velocity. This is precisely what the FLUFIX model predicts, as shown in Fig. 13. The fact that the CAPTF did not detect such high velocities is somewhat disturbing. Part of the reason could be three-dimensional effects produced by the broad 40-cm front and rear walls. On the other hand, the tracer particle may be caught in clusters or clumps of aggregated solids. Both of these effects would lower the experimental solids velocity. An independent velocity measurement, such as that described by Drennen in the Podolski *et al.* [2] paper would be most welcome. On the other hand, the predicted solids velocities may be too high due to the lack of inclusion of lift forces in the model, which would cause solids to move from regions of high shear to low shear [17].

## Conclusions

Ensemble- and time-averaged solids velocities have been measured in a thin, two-dimensional fluidized bed, containing a simulated triangular-pitch tube array of five round cylinders, and analyzed using the hydrodynamic model of fluidization. For the first time to the authors' knowledge, the experimental and computed solids motion in a bubbling fluidized bed with simulated tube banks have been reported in detail, both qualitatively and in terms of velocities for the case of uniform superficial air velocity. Quantitatively, as shown in Fig. 12, there is a very good agreement between predicted and experimental values of axial solids velocities along the vertical line $x=31.75$ cm. However, at $x=25.4$ cm (Fig. 13), solids velocities are overpredicted in the vicinity of the tubes. Inclusion of lift forces and/or three-dimensional effects in the model may resolve this discrepancy. The predicted solids velocities in the vicinity of the tubes do agree with inferred solids velocities determined from the power spectra of the pressure fluctuations. The major frequencies predicted from the computer simulation and those obtained from the experiment agree and lie in a narrow range of 2–3 Hz.

## Acknowledgements

This work was partially supported by the U.S. Department of Energy, Assistant Secretary for Fossil Energy, Morgantown Energy Technology Center, under contract No. W-31-109-ENG-38, and by the Cooperative Research and Development Venture, 'Erosion of FBC Heat Transfer Tubes'. Members of the Venture are the U.S. Department of Energy, Morgantown Energy Technology Center; Electric Power Research Institute; State of Illinois Center for Research on Sulfur In Coal; Foster Wheeler Development Corp.; ASEA Babcock PFBC; ABB Combustion Engineering Inc.; Tennessee Valley Authority; and Argonne National Laboratory. The UIUC work was sponsored by the Illinois Department of Energy and Natural Resources through its Coal Development Board and Center for Research on Sulfur in Coal.

## List of symbols

| | |
|---|---|
| $c$ | compaction modulus |
| $d_p$ | particle diameter, m |
| $G$ | solids elastic modulus, Pa |
| $\vec{g}$ | acceleration due to gravity, m $s^{-2}$ |
| $\bar{\bar{I}}$ | unit tensor |
| $L_j$ | number of tracer's occurrences per hour |
| $n$ | number of phases |
| $P$ | pressure, Pa |
| $t$ | time, s |
| $U$ | superficial air velocity, m $s^{-1}$ |
| $U_{mf}$ | minimum fluidizing velocity, m $s^{-1}$ |
| $V_{xj}$, $V_{zj}$ | $x$ and $z$ components of tracer's velocity |
| $\vec{v}$ | velocity vector, m $s^{-1}$ |

*Greek letters*

| | |
|---|---|
| $\bar{\bar{\beta}}_{ik}$ | fluid-particle friction coefficient tensor, kg $(m^3\ s)^{-1}$ |
| $\delta_{ksi}$ | Kronecker delta function given by eqn. (4) |
| $\epsilon$ | gas volume fraction |
| $\epsilon_s$ | solids volume fraction $=1-\epsilon$ |
| $\epsilon^*$ | compaction gas volume fraction |

| | |
|---|---|
| $\theta$ | direction of the velocity vector as measured in the counterclockwise direction from the positive direction of the $x$ axis, deg |
| $\bar{\bar{\sigma}}_{ke}$ | effective stress defined by eqn. (3) |
| $\rho$ | density, kg $m^{-3}$ |
| $\rho_s$, $\rho_g$ | solids and gas phase densities, respectively, kg $m^{-3}$ |
| $\bar{\bar{\tau}}_{kc}$ | coulombic stress for solids ($k=s$), Pa |
| $\bar{\bar{\tau}}_{kv}$ | microscopic viscous phase stress, Pa |
| $\mu_k$ | microscopic viscosity, Pa s (1 Pa s = 10 poise) |

*Subscripts*

| | |
|---|---|
| i, k | phase i, k |
| j | number of subset |
| s | solids phase |
| g | gas phase |

*Operators*

| | |
|---|---|
| $\nabla\cdot$ | divergence |
| $\nabla$ | gradient |

## References


1 J. S. Lin, M. M. Chen and B. T. Chao, *AIChE J., 31* (1985) 465.

2 W. F. Podolski, R. W. Lyczkowski, E. Montrone, J. Drennen, Y. H. Ai and B. T. Chao, in E. J. Anthony (ed.), *Proc. 11th (1991) Int. Conf. Fluidized Bed Combustion,* Vol. 2, American Society of Mechanical Engineers, New York, 1991, pp. 609–618.

3 R. W. Lyczkowski, S. Folga, S. L. Chang, J. X. Bouillard, C. S. Wang, G. F. Berry and D. Gidaspow, in A. M. Manaker (ed.), *Proc. 10th (1989) Int. Conf. Fluidized Bed Combustion,* Vol. 1, American Society of Mechanical Engineers, New York, 1989, pp. 465–478.

4 S. W. Burge, *FORCE2-A Multidimensional Flow Program for Gas Solids flow, Theory Guide and User's Guide,* Babcock & Wilcox, Alliance, Ohio, May 1991.

5 J. Ding and R. W. Lyczkowski, *Powder Technol., 73* (1992) 127.

6 R. W. Lyczkowski and J. X. Bouillard, *Users Manual for FLUFIX/MOD2: A Computer Program for Fluid-Solids Hydrodynamics,* Argonne National Laboratory Report, Argonne, IL, April 1992.

7 Y. H. Ai, *M.S. Thesis,* University of Illinois, Urbanna–Champaign, IL, 1990.

8 J. M. D. Merry and J. F. Davidson, *Trans. Inst. Chem. Eng., 51* (1973) 361.

9 J. H. Nielsen and A. Gilchrist, *Wear, 11* (1968) 111.

10 O. Sitnai and A. B. Whitehead, in J. F. Davidson, R. Clift and D. Harrison (eds.), *Fluidization,* Academic Press, London, 2nd edn., 1985, pp. 473–493.

11 J. X. Bouillard, R. W. Lyczkowski, S. Folga, G. F. Berry and D. Gidaspow, *Can. J. Chem. Eng., 67* (1989) 218.

12 D. Gidaspow, *Appl. Mech. Rev., 39* (1986) 1.

13 J. X. Bouillard, R. W. Lyczkowski and D. Gidaspow, *AIChE J., 35* (1989) 908.

14 R. Jackson, in J. F. Davidson, R. Clift and Harrison (eds.), *Fluidization,* Academic Press, London, 2nd edn., 1985, pp. 47–72.

15 K. Rietema, *The Dynamics of Fine Powders,* Elsevier, London and New York, 1991, pp. 166–173.

16 B. Singh, T. G. Callcott and G. R. Rigby, *Powder Technol., 20* (1978) 99.

17 M. R. Davidson, *Appl. Math. Modelling, 14* (1990) 67.